JOURNAL OF SYNCHROTRON RADIATION

ISSN 1600-5775

Received 29 October 2015
Accepted 21 July 2016

Edited by G. Grübel, HASYLAB at DESY, Germany

‡ Current address: Faculty of Health and Institute of Health and Biomedical Innovation, Queensland University of Technology, Queensland 4000, Australia.

Keywords: X-ray fluorescence; scanning X-ray diffraction microscopy; ptychography.

Supporting information: this article has supporting information at journals.iucr.org/s

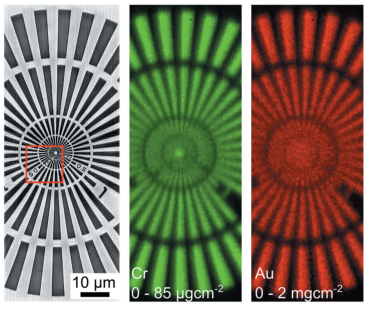

Simultaneous X-ray fluorescence and scanning X-ray diffraction microscopy at the Australian Synchrotron XFM beamline

Michael W. M. Jones,[a,b]*‡ Nicholas W. Phillips,[b,c] Grant A. van Riessen,[d] Brian Abbey,[b] David J. Vine,[e] Youssef S. G. Nashed,[f] Stephen T. Mudie,[a] Nader Afshar,[a] Robin Kirkham,[g] Bo Chen,[b] Eugeniu Balaur[b] and Martin D. de Jonge[a]*

[a]Australian Synchrotron, 800 Blackburn Road, Clayton, Victoria 3168, Australia, [b]ARC Centre of Excellence in Advanced Molecular Imaging, La Trobe Institute for Molecular Sciences, La Trobe University, Victoria 3086, Australia, [c]CSIRO Manufacturing, Parkville, Victoria 3052, Australia, [d]Department of Chemistry and Physics, La Trobe Institute for Molecular Science, La Trobe University, Victoria 3086, Australia, [e]X-ray Science Division, Advanced Photon Source, Argonne National Laboratory, Argonne, IL 60439, USA, [f]Mathematics and Computer Science Division, Argonne National Laboratory, Argonne, IL 60439, USA, and [g]CSIRO Manufacturing, Clayton, Victoria 3168, Australia. *Correspondence e-mail: mw.jones@qut.edu.au, martin.dejonge@synchrotron.org.au

Owing to its extreme sensitivity, quantitative mapping of elemental distributions *via* X-ray fluorescence microscopy (XFM) has become a key microanalytical technique. The recent realisation of scanning X-ray diffraction microscopy (SXDM) meanwhile provides an avenue for quantitative super-resolved ultrastructural visualization. The similarity of their experimental geometries indicates excellent prospects for simultaneous acquisition. Here, in both step- and fly-scanning modes, robust, simultaneous XFM-SXDM is demonstrated.

1. Introduction

X-ray fluorescence microscopy (XFM) provides exquisite sensitivity allowing measurement of trace-elemental distributions at a resolution determined by the incident probe size (De Samber *et al.*, 2010; Jones *et al.*, 2015; Hare *et al.*, 2015; Fahrni, 2007). By scanning the sample with respect to the probe, XFM can generate quantitative two-dimensional elemental maps, offering insights into sample structure and function which are unobtainable *via* any other means. The Maia detector system (Siddons *et al.*, 2014) at the XFM beamline at the Australian Synchrotron (Paterson *et al.*, 2011) allows rapid imaging of large samples, largely due to the specific experimental geometry, the large detector solid angle, and close integration of scanning and fluorescence data channels (Kirkham *et al.*, 2010). The high efficiency of X-ray fluorescence detection allows for samples to be imaged quickly 'on-the-fly', important for covering large sample areas (Jones *et al.*, 2015).

Using the same scanning geometry as XFM, but collecting the transmitted coherent diffraction signal from overlapping regions of the sample, a super-resolution quantitative image may be iteratively recovered. This method is generally referred to as 'ptychography' (Rodenburg *et al.*, 2007), and when the sample sits within the focal plane of a lens or other focusing device the technique is described as scanning X-ray diffraction microscopy (SXDM) (Thibault *et al.*, 2008). In addition to providing a quantitative image of the sample, the illumination function can also be reconstructed (Thibault *et al.*, 2009), allowing simultaneous characterization of both

sample and probe. Furthermore, it has recently been demonstrated that effects such as partial coherence of the incident illumination (Chen *et al.*, 2012), sample vibrations or positional inaccuracies (Thibault & Menzel, 2013; Clark *et al.*, 2014*a*) can be accounted for through use of modal decomposition for the propagation of the diffracting wavefield. Recently, SXDM has also been demonstrated in fly-scanning mode (Clark *et al.*, 2014*b*; Huang *et al.*, 2015; Pelz *et al.*, 2014; Deng *et al.*, 2015*a*), allowing data collection times comparable with the fast-scanning Maia detector system.

As XFM and SXDM share similar experimental conditions and provide complementary quantitative information, it is natural that they are combined in a single simultaneous measurement (Schropp *et al.*, 2010; Deng *et al.*, 2015*b*). When combined, SXDM provides ultrastructural context for the elemental imaging (Vine *et al.*, 2012; Deng *et al.*, 2015*c*). However, when the X-ray fluorescence detector is placed at 90° to the incident beam (Deng *et al.*, 2015*c*), the sample is usually rotated to allow efficient escape of fluorescent photons. For some samples, this rotation can result in the 'smearing' of high-aspect features in one or both images (Schropp *et al.*, 2010). This effect can be eliminated where fluorescence data are collected with the sample at normal incidence to the beam, such as the Maia detector (Siddons *et al.*, 2014) and the low-energy fluorescence detection scheme at TwinMic (Gianoncelli *et al.*, 2009). In this paper we report on the first simultaneous XFM-SXDM experiments at the XFM beamline at the Australian Synchrotron implemented in both step- and fly-scanning modes. We describe the integration of SXDM data collection with event-mode XFM data acquisition, allowing seamless data handling for robust and efficient SXDM image reconstruction and paving the way to routine simultaneous SXDM and XFM data collection at the Australian Synchrotron.

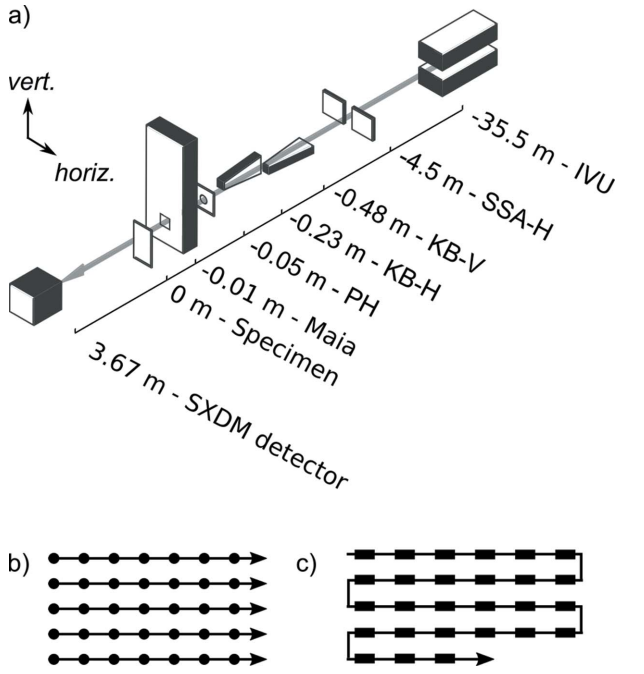

Figure 1
Simplified schematic of the experimental arrangement for simultaneous collection of SXDM and XFM data (*a*). An in-vacuum undulator (IVU) and horizontal secondary-source aperture (SSA-H) define the vertical and horizontal source positions. A KB mirror pair is used to create a 2.5 µm focus, while a 100 µm pinhole (PH) 5 cm upstream of the focus, combined with the aperture through the Maia detector, remove parasitic scatter from upstream optics. The EIGER 1M detector was placed 3.67 m downstream of the focus with a He-filled flight tube (not shown) installed between the specimen and the EIGER detector to reduce air scatter. All distances are relative to the focus in metres. For simplicity, some upstream optics are not shown and the figure is not to scale. Step- and fly-scan trajectories are shown in (*b*) and (*c*), respectively, with the points in (*b*) representing the sampling locations and the boxes in (*c*) representing the extended trajectories over which diffraction data were acquired.

2. Method

X-rays with an incident energy of 10 keV were focused to a spot of approximately 2.5 µm FWHM with a Kirkpatrick–Baez (KB) mirror pair (see Fig. 1*a*). A 100 µm pinhole prevented unwanted mirror scatter from reaching the focal plane. An in-vacuum undulator (IVU) defines the vertical source position, while a horizontal secondary source aperture (SSA-H) defines the horizontal source position at 4.5 m upstream of the focus. A horizontal focusing mirror midway between the IVU and SSA-H re-images the horizontal source to the SSA-H, with white-beam slits 17 m upstream of the SSA-H set to 1.1 mm × 0.2 mm (horizontal × vertical). To provide a spatially coherent beam at the focus, the SSA-H was set to 2.5 µm, with the full vertical beam accepted from the IVU delivering approximately 4×10^7 photons s^{-1} to the sample with four spatially coherent modes in the ideal case. Diffraction data were collected using an EIGER X 1M detector with 75 µm square pixels, placed 3.67 m downstream of the focus, with a He-filled flight tube used to reduce air scatter and absorption between the sample and EIGER detector. Fluorescence data were collected simultaneously using a 384-element Maia (Revision C) detector (Siddons *et al.*, 2014) placed in its usual backscatter geometry.

The object imaged in this work was scanned in the focal plane of the KB mirrors with 100 nm encoded stages in both the horizontal and vertical directions. We used a Siemens star test pattern comprising 450 nm of electro-deposited Au patterned using electron beam lithography (EBL). Before lift-off of the EBL resist, a continuous 60 nm film of Cr was formed through physical vapour deposition. After lift-off of the EBL resist, only the Cr deposited onto the Au regions remains, resulting in a layered Au–Cr pattern. The pattern was manufactured on a 100 nm-thick silicon nitride film residing on a silicon substrate. Afterwards, a back-etching of Si was performed to expose the free-standing silicon nitride film with Au–Cr features. At 10 keV, the expected phase change due to this thickness of material is approximately equal to 0.73 rad, dominated by the Au layer. The Cr layer was used to provide ready access to fluorescence images at energies down to 5.9 keV.

Data were collected in two different modes of acquisition: 'step scan' and 'fly scan'. In step-scan mode, the specimen was translated in a raster scan as shown in Fig. 1(*b*) with a sampling

interval equal to 500 nm in both the horizontal and vertical directions, with a software-triggered exposure time equal to 22.5 ms per frame. An additional 220 ms settling time per step was included to minimize the effects of residual stage motion. As the sample shutter remains open, the Maia detector acquired data for a total of around 242.5 ms per position. Accordingly, the total XFM imaging time was 2.8 h while the SXDM imaging time was approximately 8.7 min with respective imaging doses of 7.2×10^5 and 7.4×10^4 Gy. In step-scan mode, the image was collected at a mean rate of 0.64 $\mu m^2 s^{-1}$, including settling time.

In fly-scan mode the specimen was translated continually in the horizontal direction at a velocity of 20 $\mu m s^{-1}$. The scanning points traced out a serpentine trajectory as shown in Fig. 1(*c*). The Maia detector system was configured to generate hardware pixel triggers for every 400 nm of sample movement, which both delineated the fluorescence image pixels and triggered the EIGER detector to acquire diffraction data. With each received trigger, the EIGER detector acquired a 10 ms exposure, corresponding to 200 nm of sample movement, with no diffraction data collected over the remaining 10 ms/200 nm. This 10 ms 'dead-time' between data acquisition removed the possibility of residual stage motion (such as vibration or velocity inconsistencies) re-triggering the EIGER detector, which we discuss in more detail below. The total scan time was approximately 12 min. Dead-time (between SXDM exposures) and end-of-line overheads result in an SXDM imaging time of approximately 4.6 min. In this case, the respective imaging doses for the XFM and ptychography datasets were 9.3×10^4 and 4.6×10^4 Gy. In fly-scan mode, data were collected at a rate of 6.7 $\mu m^2 s^{-1}$, an order of magnitude faster than step scanning.

SXDM requires exacting knowledge of the sampling location of all diffraction data particularly when the reconstruction engine does not include position refinement. This becomes problematic when additional or missed camera triggers are generated and not taken into account, especially for datasets of $\sim 10^5$ diffraction frames. Depending on the triggering architecture, non-ideal behaviour, including residual motion in the specimen stage, can result in the generation of either additional or missed camera triggers at each location, depending on the exact cause. In our case, end-of-line positioner settling often resulted in multiple camera triggers. This problem can be managed either by exact and careful control of the camera triggering or by careful accounting of the acquired frames. In this experiment, we chose the latter approach, accounting for all the acquired frames by recording an acquisition-in-progress (AIP) trigger from the EIGER detector into the event-mode data stream. Using the EIGER detector system, every AIP trigger corresponded to a single diffraction frame, *i.e.* no data were lost. The total number of diffraction frames recorded was never in disagreement with the number of AIP signals recorded, showing excellent performance of both detector systems. For typical XFM imaging, all photon events are associated with their respective pixels. However, in this case we seek instead to determine the measurement coordinates of an ordered series of diffraction frames. The AIP event data stream was parsed post-acquisition to extract the required coordinates allowing us to process extremely irregular diffraction data without the need to inspect the individual diffraction frames. Although this point may seem trivial, full knowledge of the coordinates of each diffraction frame allows reliable and automatic reconstruction of images from SXDM data and is the key to the robust deployment of this measurement.

Diffraction frames were cropped to 128×128 pixels around the beam axis, and reconstructed using the ePIE algorithm (Maiden & Rodenburg, 2009) with a reconstructed SXDM pixel size equal to 47.4 nm. The entire set of diffraction frames (23184 and 27377 frames for the step scan and fly scan, respectively) was reconstructed on a single node of a cluster using two GPUs (NVIDIA M2070) on the Multi-modal Australian ScienceS Imaging and Visualization Environment (MASSIVE) (Goscinski *et al.*, 2014) using a data separation and recombination scheme (Nashed *et al.*, 2014); the reconstruction was run for 500 iterations with ten orthogonal probe modes, initialized as a Gaussian with 2.5 μm FWHM. The first probe mode was updated for each iteration from the tenth iteration, with all other modes updating from the 20th iteration with the complete reconstruction taking less than 3 h. A persistent phase gradient was corrected with a rolling-ball background subtraction with a radius of 4000 pixels in *Fiji* (Schindelin *et al.*, 2012). Fluorescence data were analysed using the dynamic analysis method in *GeoPIXE* (Ryan & Jamieson, 1993).

3. Results

The results of simultaneous SXDM-XFM imaging in both step- and fly-scan modes are presented in Figs. 2 and 3. Fig. 2 shows the SXDM reconstructed phase of the test object (*a*) alongside the fluorescent maps for Cr (*b*) and Au (*c*) for the step scan. From this comparison the increased resolution afforded by SXDM is immediately apparent: in the fluorescent maps the 0.5 μm bars are only resolved at their outer edge (where they approach 1 μm), while the SXDM images clearly show the entire 100 nm bar (Figs. 2*d* and 3*d*). Figs. 2(*d*)–2(*f*) show magnified views of the areas indicated in Fig. 2(*a*). Fig. 3 shows corresponding results for fly-scan data collection, again highlighting the dramatically increased resolution offered through SXDM. In this case, the rapid data acquisition without settling time leads to far fewer fluorescent photons being collected (less than 10% of the total imaging time), resulting in poorer quality elemental maps. Comparison between Figs. 2(*a*) and 3(*a*) shows excellent agreement between the SXDM results in the two data collection modes, despite using less than 50% of the SXDM imaging time in fly-scan mode.

Further comparison of the SXDM data collection modes is presented in Fig. 4. Here we see excellent agreement between both step (*a*) and fly (*b*) scans, with both modes comparing favourably with a scanning electron microscope (SEM) image of the test pattern (*c*). Both SXDM data collection modes resolve the inner end of the 100 nm bars (red arrows), which in

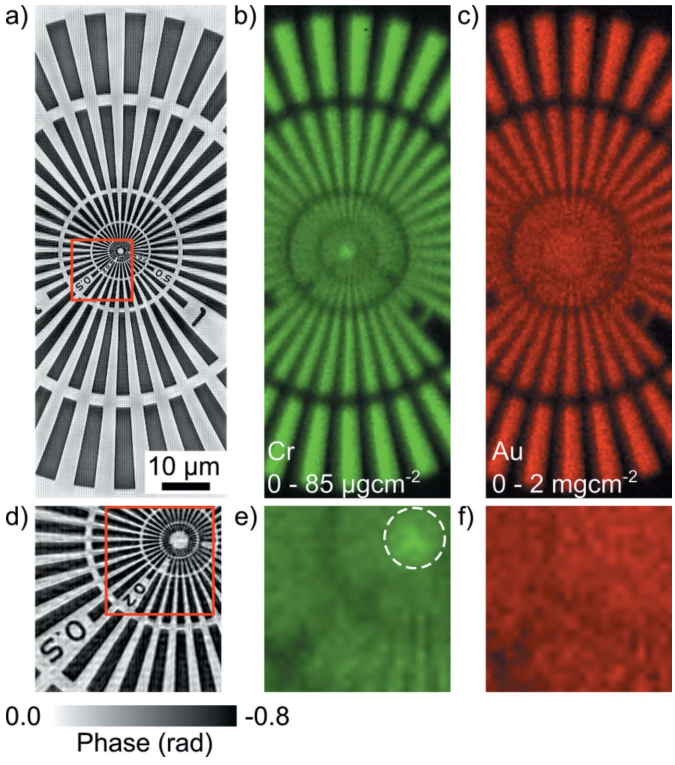

Figure 2
SXDM (*a*) and XFM maps for Cr (*b*) and Au (*c*) of the test pattern in step-scan mode, with zoomed regions in (*d*)–(*f*) taken from the box in (*a*). The increased resolution in the SXDM image is clear, with fine features clearly resolved that are not visible in the fluorescent images. A region of increased Cr fluorescence where the fabrication process failed to remove part of the patterned Cr film is visible in (*e*), highlighted with the dotted circle. The scale bar in (*a*) is equal to 10 μm.

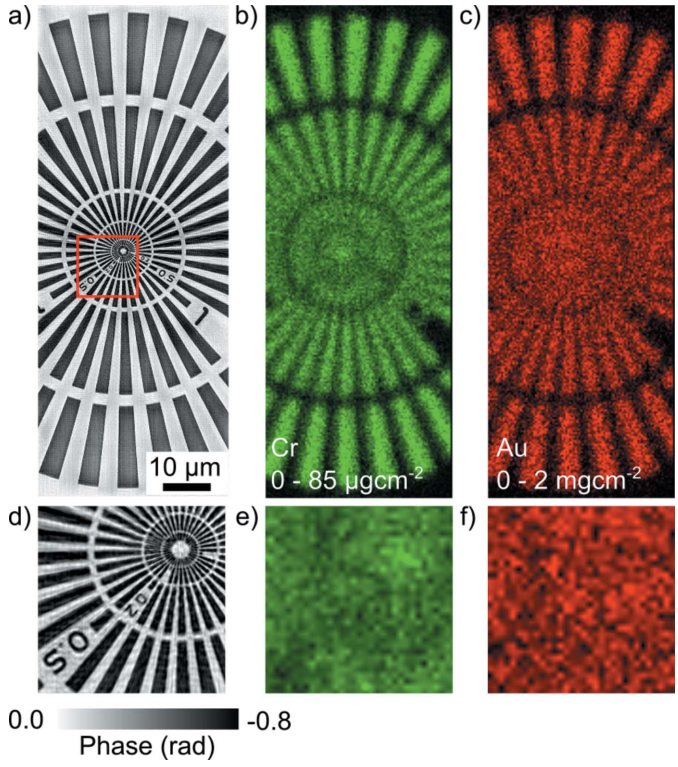

Figure 3
SXDM (*a*) and XFM maps for Cr (*b*) and Au (*c*) of the test pattern in fly-scan mode, with zoomed regions in (*d*)–(*f*) taken from the box in (*a*). Once again, we see the increased resolution in the SXDM image; however, as the total scan time is an order of magnitude faster, fewer fluorescent photons were detected, resulting in poorer fluorescent maps. The scale bar in (*a*) is equal to 10 μm.

the SEM image are hidden behind a layer of Cr that remained after fabrication [white dashed circle in Fig. 2(*e*), and red dashed circle in Fig. 4(*c*)], obscuring the innermost bars. We note that this layer of Cr is not visible in the ptychography reconstructions. With an expected phase change of 0.04 rad, it is beyond our sensitivity limit for this measurement; however, it is easily visible in the fluorescent images in Figs. 2(*e*) and 3(*e*), highlighting the complementarity of the two imaging modalities.

Line profiles across two bars of the pattern [position indicated in Fig. 4(*a*)] for the step (solid) and fly (dashed) scans are shown in Fig. 5(*a*). The profiles confirm the qualitative similarities between the results presented in Fig. 4, with the step scan showing slightly better agreement with the expected phase change of 0.73 rad. To assess the spatial resolution, the derivative of the line profiles was taken, and the full width at half-maximum (FWHM) for each slope calculated using Gaussian fitting. To determine the resolution, we averaged the FWHM for the four slopes present in the line, obtaining an experimental estimate of the resolution of 102 nm and 110 nm for the step and fly scans, respectively (Fig. 5*b*), potentially limited by an encoder resolution of 100 nm. The difference between step- and fly-scan resolution is likely due to the increased SXDM imaging time for the step scan resulting in a larger number of photons being collected (higher imaging dose), but may also be due to deviations in the assumed transit across the specimen in fly-scan mode, eliminated in step-scan

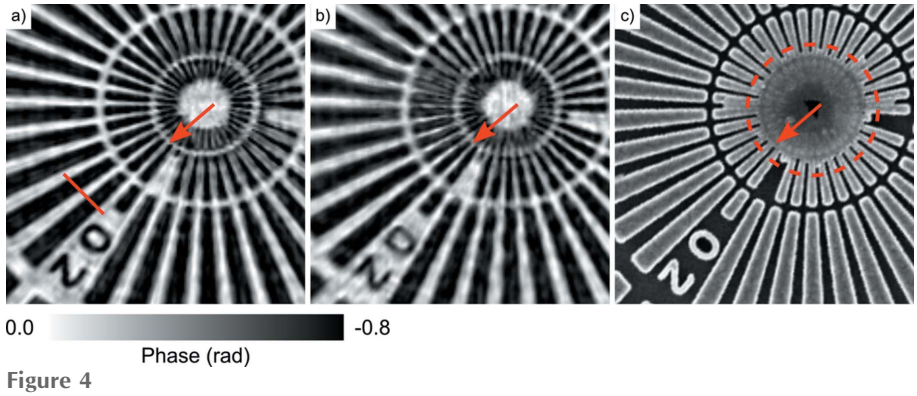

Figure 4
Magnified view of the reconstructed phase of the transmission function resulting from (*a*) step and (*b*) fly scans, with a comparison with an SEM (*c*) of the specimen, taken from the box in Fig. 2(*d*). We can clearly see the inner end of the 100 nm bar (arrows). The circle in (*c*) highlights the 60 nm layer of Cr which remained after manufacture; however, the SXDM images clearly resolve the Au beneath.

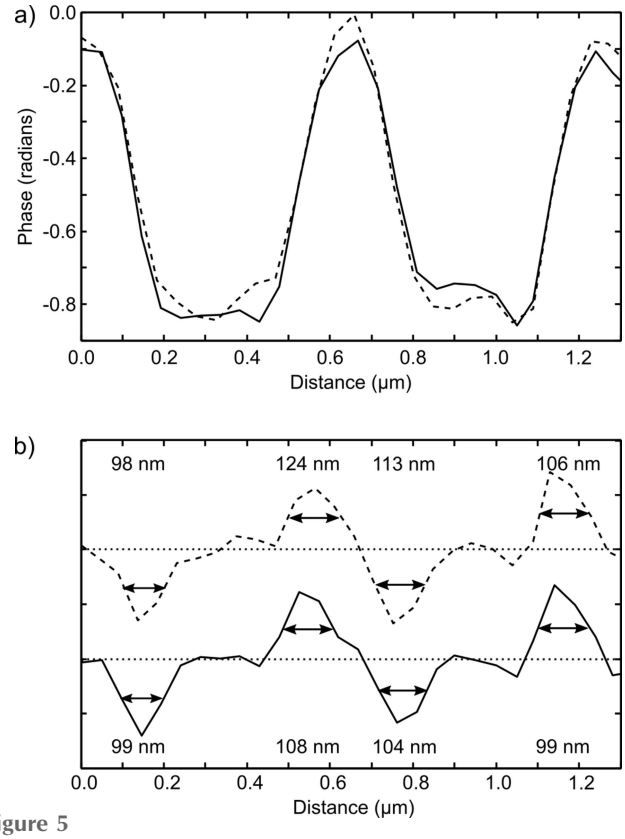

Figure 5
Line profiles (*a*) comparing the step and fly scans (solid and dashed line in each case) at the position indicated by the line in Fig. 4(*a*). Both profiles are in good agreement. The derivative of the line profiles and the Gaussian-fitted FWHM of the four steps are shown in (*b*). We obtain an estimate of the resolution from the mean of the four FWHM at 102 nm and 110 nm for the step and fly scans, respectively.

mode by the long settling time. Typically a measure of the power spectrum density is used for resolution quantification. In this case, however, we find that the power spectrum does not show noise levels exceeding the signal and therefore an assessment of the resolution cannot be obtained through these methods. This is expected as the resolution obtained from line profiles [Fig. 5(*a*) and 5(*b*)] corresponds to only two real-space resolution elements.

The reconstructed probe function is shown in Fig. 6, with the first three modes, together with the total probe intensity shown in Figs. 6(*a*)–6(*b*) and Figs. 6(*c*)–6(*d*) for the step (Fig. 2) and fly (Fig. 3) scans, respectively. Comparison between the total probe intensity for the step and fly scans [Figs. 6(*b*) and 6(*d*)] shows the effects of probe broadening in the fly scan (Deng *et al.*, 2015*a*), although in this case the effect is minor as the transit per exposure was 200 nm (less than 10% of the probe width). The relative power distribution between the probe modes is relatively even as seen in Fig. 5(*e*), with significant power in the tenth probe mode. It is important to compare and contrast this behaviour with that reported in the literature. While in the present case we did not explore the effects of sampling density, Pelz *et al.* (2014) report that this can lead to a similar power distribution as that observed here. However, Pelz *et al.* (2014) also reported that sparse sampling density has a detrimental effect on fly-scan image quality while step-scan image quality remains high. Comparing the power distribution in the probe modes from Pelz *et al.* (2014) with ours, we find that in contrast to Pelz *et al.* (2014) ours is similar for both step- and fly-scan modes (Fig. 5*e*) with similarly high image quality (Figs. 2 and 3) obtained from each scan mode. This suggests that sparse sampling is not likely to be the cause of the even power distribution in the present case. In addition, analysis of the static fringe visibility indicates that the spatial coherence length is comparable with the probe diameter and therefore unlikely to cause the even probe power distribution; indeed a total of four spatially coherent probe modes are present in the ideal case. Analysis of the beam intensity delivered to the sample during the scan showed that the intensity varied by less than 0.05% over the course of the scans, and therefore is unlikely to result in the power distribution of the probe modes observed.

This process of elimination leads us to conclude that the gradual decrease in the power within the modes observed here is likely due to residual stage motion. The addition of a fixed vibration pattern in the sample has been shown to reduce the power in the first mode by approximately 50%, while increasing the relative power in higher-order probe modes (Clark *et al.*, 2014*a*). However, unlike the fixed vibrations described by Clark *et al.* (2014*a*), in our case we have much greater variability in our motion, which is constrained only to within 100 nm. We believe it is the variability of the sample

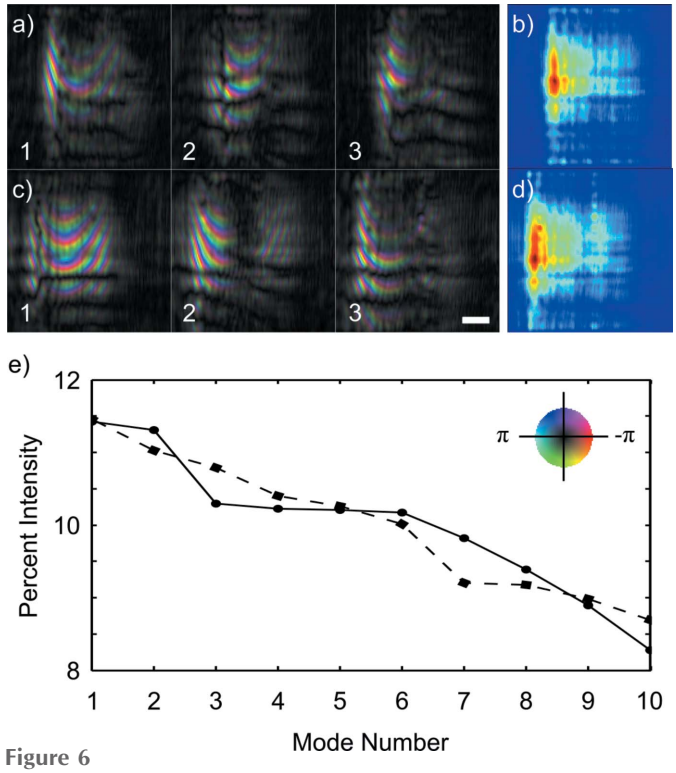

Figure 6
The first three probe modes and the total probe intensity for the step (*a*)–(*b*) and fly (*c*)–(*d*) scans, respectively. Phase and magnitude are encoded as hue and brightness as depicted in the colour wheel in (*e*). The scale bar in (*c*)-3 is equal to 1 μm. The probe in the fly scan is broadened compared with the step scan by the distance traversed during each exposure as expected (Deng *et al.*, 2015*a*). The distribution of probe power across all ten modes is shown in (*e*) for step (solid) and fly (dashed) scans.

motion, which manifests as a decoherence of the imaging system (Thibault & Menzel, 2013), that gives rise to the broader power distribution across probe modes in the present case. It may be expected that reconstruction quality should increase by including additional probe modes; however, line profile analysis of the reconstructions using 50 probe modes show no measurable improvement in either the resolution or contrast (see Fig. S1 of the supporting information), suggesting that our relatively unknown motion kernel is the limiting factor in our reconstruction quality. We anticipate that, as the motion kernel of the specimen becomes more accurately known through improved stage control, this motion will no longer limit our reconstruction quality and the addition of further probe modes will improve our results with fewer probe modes required to fully describe the system.

4. Discussion and conclusions

We have demonstrated simultaneous X-ray fluorescence and scanning X-ray diffraction microscopy in both step- and fly-scan modes at the XFM beamline at the Australian Synchrotron. The results obtained for step and fly scanning are in excellent agreement, with the reduced overheads from fly scanning offering significant efficiency gains in data collection with only minor resolution penalties. Incorporating the AIP signal into the event-mode data stream allowed the SXDM data to be robustly and automatically organized, providing efficient analysis of large datasets. With this method of SXDM data collection and organization we anticipate acquisition of diffraction data in 'free-run' mode, where no triggers are sent to the camera, but rather it is allowed to acquire at its optimum rate, with the AIP signal recorded into the event-mode data stream. This mode of operation will allow the fluorescence and diffraction data acquisition times to be decoupled from each other, with each collected at the optimum rate for their respective detectors and analysis methods. Furthermore, such operation relaxes requirements for 'perfect' stage motion, with imperfect stage motion potentially beneficial, providing the variability in diffraction data positions required to break the uniformity of the Cartesian scan grid, thus avoiding 'raster grid pathology' (Thibault *et al.*, 2009). While this demonstration used an EIGER X 1M detector, future measurements will be performed using the PIXIRAD-1 detector (Bellazzini *et al.*, 2013) with 512 × 476 55 µm hexagonal pixels.

As the two images are simultaneously collected with common experimental parameters, information can be shared between the two techniques (Vine *et al.*, 2012; Deng *et al.*, 2015*b*). We anticipate that future work in this area will lead to additional significant improvements, such as incorporating the complex transmission function obtained from SXDM directly into the calculation of the expected fluorescent yield on a per XFM pixel basis, reducing the need for *a priori* knowledge of the sample composition.

The geometry of the Maia detector allows large objects to be placed at normal incidence to the beam, eliminating the smearing of high-aspect features observed when some samples are mounted at an angle to the beam (Schropp *et al.*, 2010). This arrangement has been shown to be advantageous for large objects in XFM measurements (Jones *et al.*, 2015), and, when combined with efficient fly scanning and robust diffraction data organization through event-mode data acquisition, allows for large samples to be imaged without compromising either data acquisition modes. Using this geometry combined with the fast rate of data collection opens the door to investigating entire small animals such as *C. elegans* or undertaking population studies on many samples, rather than single specimens typically imaged through ptychography. Furthermore, we anticipate undertaking dynamic studies on materials specimens with time resolution of the order of minutes.

A planned upgrade to 20 nm encoders on the vertical and horizontal stages will reduce real-space positioning errors. It is anticipated that this upgrade will not only allow for resolution improvements but also that fewer probe modes will be required to fully describe the system. The present results were collected with a secondary source size an order of magnitude smaller than typical operation to improve the spatial coherence and ensure that the EIGER detector is within the limit of its dynamic range. To increase the incident flux on the sample without saturating the detector, we plan to implement a semi-transparent beamstop (Wilke *et al.*, 2013) and incorporate the influence of the reduced coherence under these conditions into the reconstruction algorithms (Chen *et al.*, 2012; Thibault & Menzel, 2013). Alternatively, diffraction-limited storage rings would provide an increased incident coherent flux without the need for partial coherence algorithms (de Jonge *et al.*, 2014). With these changes, we will obtain higher statistics in the fluorescent images in fly-scan mode and allow high-resolution SXDM data to be collected at a rate that is compatible with state-of-the-art fly-scan fluorescence data collection using the Maia detector, enabling these two complimentary techniques to be applied simultaneously without compromise to either.

Acknowledgements

We thank Dectris Ltd, Baden, Switzerland, for loan of the EIGER X 1M detector. This research was undertaken on the XFM beamline at the Australian Synchrotron, Victoria, Australia, and supported by the Multi-modal Australian ScienceS Imaging and Visualization Environment (MASSIVE) (http://www.massive.org.au). The authors acknowledge the support of the Australian Research Council (ARC) Centre of Excellence for Advanced Molecular Imaging. This work was performed in part at the Melbourne Centre for Nanofabrication (MCN) in the Victorian Node of the Australian National Fabrication Facility (ANFF).

References

Bellazzini, R., Spandre, G., Brez, A., Minuti, M., Pinchera, M. & Mozzo, P. (2013). *J. Instrum.* **8**, C02028.

Chen, B., Abbey, B., Dilanian, R., Balaur, E., van Riessen, G. A., Junker, M., Tran, C. Q., Jones, M. W. M., Peele, A. G., McNulty, I.,

Vine, D. J., Putkunz, C. T., Quiney, H. M. & Nugent, K. A. (2012). *Phys. Rev. B*, **86**, 235401.
Clark, J. N., Huang, X., Harder, R. J. & Robinson, I. K. (2014*a*). *Phys. Rev. Lett.* **112**, 113901.
Clark, J. N., Huang, X., Harder, R. J. & Robinson, I. K. (2014*b*). *Opt. Lett.* **39**, 6066–6069.
de Jonge, M. D., Ryan, C. G. & Jacobsen, C. J. (2014). *J. Synchrotron Rad.* **21**, 1031–1047.
Deng, J., Nashed, Y. S. G., Chen, S., Phillips, N. W., Peterka, T., Ross, R., Vogt, S., Jacobsen, C. & Vine, D. J. (2015a). *Opt. Express*, **23**, 5438–5451.
Deng, J., Vine, D. J., Chen, S., Nashed, Y. S. G., Jin, Q., Phillips, N. W., Peterka, T., Ross, R., Vogt, S. & Jacobsen, C. J. (2015c). *Proc. Natl Acad. Sci. USA*, **112**, 2314–2319.
Deng, J., Vine, D. J., Chen, S., Nashed, Y. S. G., Peterka, T., Ross, R., Vogt, S. & Jacobsen, C. (2015b). *Proc. SPIE*, **9592**, 95952DU.
De Samber, B., Silversmit, G., De Schamphelaere, K., Evens, R., Schoonjans, T., Vekemans, B., Janssen, C., Masschaele, B., Van Hoorebeke, L., Szalóki, I., Vanhaecke, F., Rickers, K., Falkenberg, G. & Vincze, L. (2010). *J. Anal. At. Spectrom.* **25**, 544–553.
Fahrni, C. J. (2007). *Curr. Opin. Chem. Biol.* **11**, 121–127.
Gianoncelli, A., Kaulich, B., Alberti, R., Klatka, T., Longoni, A., de Marco, A., Marcello, A. & Kiskinova, M. (2009). *Nucl. Instrum. Methods Phys. Res. A*, **608**, 195–198.
Goscinski, W. J., McIntosh, P., Felzmann, U. C., Maksimenko, A., Hall, C. J., Gureyev, T., Thompson, D., Janke, A., Galloway, G., Killeen, N. E. B., Raniga, P., Kaluza, O., Ng, A., Poudel, G., Barnes, D., Nguyen, T., Bonnington, P. & Egan, G. F. (2014). *Front. Neuroinform.* **8**, 30.
Hare, D. J., New, E. J., de Jonge, M. D. & McColl, G. (2015). *Chem. Soc. Rev.* **44**, 5941–5958.
Huang, X., Lauer, K., Clark, J. N., Xu, W., Nazaretski, E., Harder, R., Robinson, I. K. & Chu, Y. S. (2015). *Sci. Rep.* **5**, 9074.
Jones, M. W. M., de Jonge, M. D., James, S. A. & Burke, R. (2015). *J. Biol. Inorg. Chem.* **20**, 979–987.
Kirkham, R., Dunn, P. A., Kuczewski, A. J., Siddons, D. P., Dodanwela, R., Moorhead, G. F., Ryan, C. G., De Geronimo, G., Beuttenmuller, R., Pinelli, D., Pfeffer, M., Davey, P., Jensen, M., Paterson, D., de Jonge, M. D., Howard, D. L., Küsel, M., McKinlay, J., Garrett, R., Gentle, I., Nugent, K. & Wilkins, S. (2010). *AIP Conf. Proc.* **1234**, 240–243.
Maiden, A. M. & Rodenburg, J. M. (2009). *Ultramicroscopy*, **109**, 1256–1262.
Nashed, Y. S. G., Vine, D. J., Peterka, T., Deng, J., Ross, R. & Jacobsen, C. (2014). *Opt. Express*, **22**, 32082–32097.
Paterson, D., de Jonge, M. D., Howard, D. L., Lewis, W., McKinlay, J., Starritt, A., Kusel, M., Ryan, C. G., Kirkham, R., Moorhead, G., Siddons, D. P., McNulty, I., Eyberger, C. & Lai, B. (2011). *AIP Conf. Proc.* **1365**, 219–222.
Pelz, P. M., Guizar-Sicairos, M., Thibault, P., Johnson, I., Holler, M. & Menzel, A. (2014). *Appl. Phys. Lett.* **105**, 251101.
Rodenburg, J. M., Hurst, A. C., Cullis, A. G., Dobson, B. R., Pfeiffer, F., Bunk, O., David, C., Jefimovs, K. & Johnson, I. (2007). *Phys. Rev. Lett.* **98**, 034801.
Ryan, C. G. & Jamieson, D. N. (1993). *Nucl. Instrum. Methods Phys. Res. B*, **77**, 203–214.
Schindelin, J., Arganda-Carreras, I., Frise, E., Kaynig, V., Longair, M., Pietzsch, T., Preibisch, S., Rueden, C., Saalfeld, S., Schmid, B., Tinevez, J. Y., White, D. J., Hartenstein, V., Eliceiri, K., Tomancak, P. & Cardona, A. (2012). *Nat. Methods*, **9**, 676–682.
Schropp, A., Boye, P., Feldkamp, J. M., Hoppe, R., Patommel, J., Samberg, D., Stephan, S., Giewekemeyer, K., Wilke, R. N., Salditt, T., Gulden, J., Mancuso, A. P., Vartanyants, I., Weckert, E., Schöder, S., Burghammer, M. & Schroer, C. G. (2010). *Appl. Phys. Lett.* **96**, 091102.
Siddons, D. P., Kirkham, R., Ryan, C. G., De Geronimo, G., Dragone, A., Kuczewski, A. J., Li, Z. Y., Carini, G. A., Pinelli, D., Beuttenmuller, R., Elliott, D., Pfeffer, M., Tyson, T. A., Moorhead, G. F. & Dunn, P. A. (2014). *J. Phys. Conf. Ser.* **499**, 012001.
Thibault, P., Dierolf, M., Bunk, O., Menzel, A. & Pfeiffer, F. (2009). *Ultramicroscopy*, **109**, 338–343.
Thibault, P., Dierolf, M., Menzel, A., Bunk, O., David, C. & Pfeiffer, F. (2008). *Science*, **321**, 379–382.
Thibault, P. & Menzel, A. (2013). *Nature (London)*, **494**, 68–71.
Vine, D. J., Pelliccia, D., Holzner, C., Baines, S. B., Berry, A., McNulty, I., Vogt, S., Peele, A. G. & Nugent, K. A. (2012). *Opt. Express*, **20**, 18287–18296.
Wilke, R. N., Vassholz, M. & Salditt, T. (2013). *Acta Cryst.* A**69**, 490–497.